https://doi.org/10.1016/j.tws.2020.106946

Circular Hybrid Double-Skin Tubular Columns with A Stiffener-Reinforced Steel Inner Tube and A Large-Rupture-Strain FRP Outer Tube: Compressive Behavior

Le Huang[a], Shi-Shun Zhang[b*], Tao Yu[c, a] and Kai-Di Peng[c]

[a]*School of Civil, Mining & Environmental Engineering, Faculty of Engineering & Information Sciences, University of Wollongong, Australia.*
[b]*School of Civil Engineering and Mechanics, Huazhong University of Science and Technology, Wuhan, China. Email:* shishun@hust.edu.cn
[c]*Department of Civil and Environmental Engineering, The Hong Kong Polytechnic University, Hung Hom, Kowloon, Hong Kong, China.*

ABSTRACT

A typical fiber-reinforced polymer (FRP)-concrete-steel double-skin tubular column (DSTC) consists of an FRP outer tube, a hollow steel inner tube and an annular concrete in-fill in between. The existing studies on DSTCs in the past decade have generally confirmed the good structural performance of such column form, while it is worth noting that the possible in-ward buckling of the steel tubes in DSTCs is still a problem to be addressed, especially when DSTCs are subjected to large axial deformation. Against this background, a variation form of DSTCs called R-DSTCs has been recently developed by the authors. An R-DSTC is a DSTC in which the steel inner tube is reinforced by vertical stiffeners on the outer surface and the FRP outer tube can be circular, square or rectangular. The present paper presents the first ever experimental study on the compressive behavior of circular R-DSTCs which is the most common form of DSTCs. For the circular R-DSTC specimens tested in the present study, the outer tubes are made of a type of large-rupture-strain FRP. The vertical stiffeners on the steel inner tube are expected to delay or restrain the inward buckling of the steel tube, and the large-rupture-strain FRP outer tube makes possible a relatively large axial deformation of the specimen. In total, two DSTC specimens, twelve R-DSTC specimens and three bare steel tubes with/without stiffeners were tested, with the studied parameters covering the quantity, the dimensions and the shape of the stiffeners and the thickness of the FRP outer tube. The test results showed that R-DSTC specimens had a much better performance than the corresponding DSTC specimens in terms of both axial loading capacity and ductility, due to the existence of vertical stiffeners on the steel inner tube of R-DSTCs. The effects of the vertical stiffener-related parameters on the compressive behavior of R-DSTC specimens were also carefully examined and discussed in details.

KEYWORDS

FRP; Steel tube; Confined concrete; Double-skin; Tubular column; Stiffener; Local buckling; Large rupture strain.

1 INTRODUCTION

Fiber reinforced polymer (FRP) composites have been widely adopted as a type of confining material for concrete in structural engineering in the past two decades because of its structural advantages such as high strength, low density, excellent corrosion resistance and ease in construction [e.g., 1-9]. In addition to its most popular application of being used as externally bonded reinforcement in structural retrofitting industry, the use of FRP in new buildings and constructions has become increasingly popular in last decade [e.g., 6, 10-19]. The FRP-concrete-steel double-skin tubular column (DSTC) proposed by Ref. [10] is one of the most popular applications of FRP in new composite structural members. Typically, a DSTC is comprised of three components: an FRP outer tube, a steel inner tube and a concrete in-fill between the two tubes. The concept and the potential structural advantages of DSTCs have been well demonstrated in Ref. [10], and the extensive studies on DSTCs [e.g., 6, 10, 20-26] in the past decades have generally confirmed the good structural performance of DSTCs and developed a relatively comprehensive and in-depth understanding of the structural behavior of DSTCs. Design methods have also been provided for DSTCs in a Chinese national technical code [27]. Among the existing relevant studies, Ref. [26] tested circular DSTCs under combined axial load and cyclic lateral load, and reported that severe local buckling of the steel inner tubes of DSTC specimens in plastic hinge regions was observed as the concentrated axial deformation happened therein. Ref. [6] tested short DSTCs with a large rupture strain FRP tube under concentric compression and also found that severe local buckling of the steel inner tubes of DSTCs occurred as a result of the large axial deformation of the specimen. These experimental findings indicate that the potential local buckling of the steel inner tubes can be a problem when DSTCs are loaded under large axial deformation, especially when relatively thin steel tubes are used in DSTCs. In addition, when the bending is significant or even becomes the dominant behavior of DSTCs, the superior structural performance of DSTCs could be compromised by the relatively weak bond behavior between the concrete and steel components due to the smooth bi-material interface between them. Finally, when a small void ratio is used for DSTCs, the contribution of the steel inner tube in DSTCs to the second moment area of the cross-section can be limited as its position is close to the bending axes of the cross-section. Local buckling of steel tube is also a common problem for concrete-filled steel tubes (CFSTs) [28]. To tackle this problem, welding vertical stiffeners on the inner surface of the steel tube before pouring concrete has been investigated and proved to be effective in delaying the local buckling of the steel tube and thus improving the axial behaviour of CFSTs [29-31].

Against this background, the compressive behavior of a variation form of DSTCs, namely DSTCs with a stiffener-reinforced steel inner tube (referred to as R-DSTCs hereafter for simplicity), is investigated in the present study. In R-DSTCs, the vertical stiffeners are attached on the outer surface of the steel inner tubes by welding. Due to the similar cross-sectional configurations of R-DSTCs and DSTCs, R-DSTCs obviously have all the structural advantages of DSTCs. In addition, R-DSTCs have the following structural advantages over DSTCs: (1) the inward local buckling of the steel inner tube can be delayed or restrained due to the presence of vertical stiffeners which are encased in the annular confined concrete core; (2) the concrete-steel bond behavior can be improved as the adhesion and interaction between them are enhanced by the embedded stiffeners; (3) the stiffeners in R-DSTCs can make additional contributions to the second moment of area of the cross-section and thus lead to a better seismic performance of R-DSTCs. It should be pointed out that although the addition of stiffeners onto the steel inner tube in R-DSTCs may lead to a lightly complex cross section compared with traditional double-skin tubular columns, the constructional procedure of R-DSTCs will not be much influenced in practice, as the rib-reinforced steel inner tube, to be used as part of the permanent formwork for casting concrete on site, can be prefabricated in factory.

To the best knowledge of the authors, the present study is the first ever experimental investigation into the compressive behavior of circular R-DSTCs, while another work by the authors provides an experimental study on square R-DSTCs [32]. It has been found by Ref. [32] that the vertical stiffeners can largely improve the axial load capacity and axial deformation capacity of square R-DSTCs, and such improvement was found to be influenced by the layout and geometry properties of the stiffeners. It should be noted that although Ref.

[32] has shed light on the present study, the non-uniform confinement nature resulted from the use of a square FRP tube in square R-DSTCs implies that main findings from Ref. [32] cannot be directly applicable to the circular R-DSTCs (the most common form of DSTCs), in which the confinement exerted by the circular FRP tube onto concrete is circumferentially uniform. Therefore, the present study, which aims for a better and in-depth understanding of the behavior of and thus a more confident use of circular R-DSTCs, is in necessity.

In the past decade, conventional FRP (e.g., carbon FRP and Glass FRP) are most commonly employed in experimental studies of DSTCs [e.g., 10, 22, 26]. Recently, Ref. [6] conducted an experimental study on DSTCs of which the FRP tubes were made from a type of large rupture strain FRP, namely polyethylene terephthalate (PET) FRP. PET FRP has a rupture strain of over 7%, which is over three times of the rupture strain of conventional FRP. Additionally, PET FRP is a type of environment-friendly material as it can be made from waste PET plastic products (e.g., plastic bottles). Relevant studies [e.g., 6, 15, 17, 33-37] have shown that PET FRP can substantially enhance the deformation capacity and ductility of confined concrete owing to its large rupture strain. In this regard, PET FRP tubes were adopted for all the double skin tubular columns tested in the present study to investigate the buckling behavior of the steel inner tube under large axial deformation.

In this paper, short circular R-DSTCs with a PET FRP tube were tested under concentric compression to obtain a better understanding of the compressive behavior of such columns. The studied parameters include the quantity, the dimensions and the shape of the stiffeners, and the thickness of the FRP tubes. Based on the test results, the compression behavior of R-DSTCs are discussed and interpreted in this paper.

2 EXPERIMENTAL PROGRAM

2.1 Test Specimens

A total of 14 specimens were tested in the present study, including one pair of short DSTC specimens and six pairs of short R-DSTC specimens. The two specimens in each pair were nominally identical to each other and thus had the same cross-sectional configuration, which leads to seven different cross-sectional configurations in total in this study. The typical schematic diagrams of DSTC specimens and R-DSTC specimens with four stiffeners and six stiffeners are shown in Fig. 1. All the DSTC and R-DSTC specimens in this study had an outer diameter of 240 mm (not including the thickness of the FRP outer jacket) and a height of 600 mm. The steel tubes in the DSTC and R-DSTC specimens all had an outer diameter of 168.4 mm and a thickness of 4.8 mm. In addition, three bare steel tubes having the same dimensions, two of which were reinforced with stiffeners and one was not, were also tested in the current study. The bare steel tube without stiffeners corresponded to the steel tubes in DSTC specimens, while the other two bare steel tubes reinforced with stiffeners corresponded to those in R-DSTC specimens. The studied parameters include the quantity of the stiffeners, the thickness of the stiffeners, the width of the stiffeners, the shape of the stiffeners and the thickness of the FRP tubes.

Each specimen in the present study was given a name for ease of reference. The two identical DSTC specimens were named as D-3-I and D-3-II respectively, with the letter "D" representing DSTC, the number "3" representing the quantity of plies of PET fibre sheets in the FRP tubes and the Roman numerals "I" and "II" representing the two nominally identical specimens in each pair. The name of the R-DSTCs starts with "RD" to represent R-DSTC; followed by a number (i.e., 4 or 6) to represent the quantity of stiffeners, two capital letters (i.e., AW, BW, BN and BS) to represent the dimensions of the stiffeners ("A" and "B" represent respectively the thin stiffeners with a thickness of 3mm and the thick stiffeners with a thickness of 5 mm, "W" and "N" represent respectively the wide stiffeners with a width of 32 mm and the narrow stiffeners with a width of 16 mm, and "S" means that the stiffeners are in "wave-shape" as shown in Fig. 2 with the maximum width being 32mm and the minimum width being 16mm), a number (i.e., 3 or 4) to represent the quantity of plies of PET fibre sheets in the FRP tubes, and finally a Roman numeral (i.e., I or II) to represent the two nominally identical specimens in each pair. For instance, RD-4AW-3-I refers to the first specimen of the two identical R-DSTC specimens, which has 4 stiffeners with a width of 32 mm (wide stiffeners) and a thickness of 3 mm (thin stiffeners), and a FRP tube consisting of 3 plies of FET fibre sheets. Each of the three bare steel tubes was also given a name, with "ST" referring to the steel tube without stiffener and "RST" referring to the steel tubes reinforced with vertical stiffeners. The number (i.e., 4 or 6) following "RST" represents the quantity of stiffeners on the steel tube. The key information of all the specimens is listed in Table 1.

2.2 Material Properties

The specimens were all cast using the same batch of ready-mixed self-compacting concrete. Concrete cylinders (150mm×300mm) were also cast and tested under axial compression to obtain the strength of concrete according to [38]. The compressive cylinder strength of concrete at the 28th day was found to be 32.0 MPa. Compression tests of 150mm×300mm concrete cylinders were also conducted at both the beginning and the end of the experiment. The obtained compressive cylinder strength and the strain corresponding to the strength in this period were 36.9 MPa and 0.0025, respectively, according to the test results.

The steel tubes in the current study were cut from one piece of long steel tube. The steel stiffeners were cut from the same batch of steel flat bars with the required thickness (i.e., 3 mm or 5 mm). For the steel tube and each type of flat bar, two steel coupons were cut along the longitudinal direction and tensile tests were conducted on these steel coupons according to [39]. Fig. 3 shows the stress-strain curves of steel based on the coupon test results, and the detailed material properties of the steel tube and the flat bars are listed in Table 2.

Six PET FRP coupons were prepared and tested under axial tension according to [40] to obtain the material properties of PET FRP. The stress-strain curves of PET FRP based on the coupon test results are plotted in Fig. 4, with the stress calculated by using the nominal thickness of the PET fiber sheet (i.e., 0.819 mm per ply) provided by the manufacturer. The average tensile strength and the rupture strain obtained from the coupon tests were 928.11 MPa and 0.0981, respectively.

2.3 Preparation of Specimens

Circular polyvinyl chloride (PVC) tubes having a 240 mm inner diameter were adopted as the outer formwork of the specimens for casting concrete. The PVC tubes were first mounted on a wooden base board, and then the steel tubes were concentrically placed into the PVC tubes. The seams between the base board and the bottom of PVC tubes and steel tubes were well sealed with silicone gel to avoid water leaking. The strain gauges attached on the steel tubes were well protected and the strain gauge wires were well arranged. Concrete was then cast in the space between the PVC tube and the steel tube for each specimen and the PVC tubes were removed after two weeks' curing of concrete. Resin-impregnated PET fiber sheets were wrapped on concrete via the wet lay-up method in such way that PET fibers were oriented only in the hoop direction and an overlapping zone of 150 mm in length was left in the FRP jacket of each specimen. Though prefabricated FRP tubes are preferred for DSTCs and R-DSTCs in practice, existing literatures [e.g., 41] have shown that there is little difference between using prefabricated FRP tubes directly as formwork and wrapping resin-saturated fibre sheet on hardened concrete via wet-layup method. Additional two layers of PET fiber sheets of 40mm width were wrapped at the two ends of each specimen to avoid local failure at the end regions. Fig. 5 shows the photos of specimens in preparation.

2.4 Test Set-up and Instrumentation

All the tests were conducted at the University of Wollongong using the 500 ton AVERY test machine. The axial load was applied under displacement control with a loading rate of 0.6 mm/min for all the specimens. Two linear variable displacement transducers (LVDTs), which were opposite to each other along the circumference, were used to measure the overall shortening of the specimens and another two LVDTs (also opposite to each other along the circumference) were mounted on the specimen to measure the shortening of the 150 mm-long region at the mid-height of the specimen. In addition, a small-size video camera with a light was put inside the steel tubes (at the top end) to monitor the local buckling deformation of the steel tubes in both DSTCs and R-DSTCs in the testing process. Fig. 6 shows the layout of the LVDTs and the position of camera in the test.

Three strain gauges of 20mm in gauge length were applied on the PET FRP tubes at the mid-height and evenly along the circumference (outside of the overlapping zone) to measure the hoop strains (see Fig. 7). For the steel tubes in DSTCs, two strain gauges of 10 mm in gauge length were applied on the outer surface at the mid height (180 degree apart from each other along the circumference) to measure the axial strains; for the stiffener-reinforced steel tubes in R-DSTCs, two more strain gauges of 10 mm in gauge length were attached on the stiffeners at the mid height to record the axial strains (see Fig. 7). In the tests, the axial load, the LVDTs readings, the strain gauge readings and the video from the camera were well synchronized for ease of data analyses.

3 RESULTS AND DISCUSSIONS

3.1 Failure Modes

3.1.1 DSTC and R-DSTC Specimens

Fig. 8 shows the typical failure modes of the DSTC and R-DSTC specimens. Most of the specimens failed by rupture of the FRP outer tubes near the mid height, as shown in Figs. 8(a)-(c). Loud and sharp noises were heard at the failure of the specimens. For some specimens, local debonding of the outermost layer of FRP sheet was also observed within the overlapping zone along with the rupture, as shown in Fig. 8(d). Such local debonding of FRP happened at the very late stage of the tests thus is thought to have negligible effect on the test results.

3.1.2 Bare Steel Tubes under Axial Compression

Compression tests of the three bare steel tubes were terminated when severe local buckling was observed. Fig. 9 shows the failure modes of ST, RST-4 and RST-6 at an axial shortening (at the termination of the tests) of 27.0 mm, 40.3 mm and 41 mm respectively. It can be seen from Figs. 9(a)-(b) that both the steel tube without stiffener (ST) and the steel tube reinforced with 4 stiffeners (RST-4) buckled in a typical “elephant foot” failure mode, with the “elephant foot” of the latter being less noticeable although the corresponding axial shorting of the latter is much larger. It can be seen from Fig. 9(c) that the steel tube reinforced with 6 stiffeners (RST-6) buckled at the mid-height with no “elephant foot” near the end, which is completely different from that of ST and RST-4. From the above observations, it can be seen that the stiffeners on the steel tubes have large effects on the buckling behavior of the steel tube.

3.1.3 Steel Tubes in DSTCs and R-DSTCs

By removing the FRP and concrete after test, the failure modes of steel tubes in DSTC and R-DSTC specimens were examined, and the typical failure modes are shown in Figs. 10 and 11 respectively. It is evident in Fig. 10 that the steel tubes in both D-3-I and D-3-II buckle severely but the buckling modes of the two steel tubes are somewhat different: the buckling ripples of the steel tube in D-3-I are located near the mid height, while that of the steel tube in D-3-II are located near the middle of the upper half part of the steel tube. Figs. 11(a)-(c) show the three typical failure modes of the steel tubes in R-DSTC specimens. It can be seen that the shapes of the buckling ripples of specimens with flat stiffeners (i.e., RD-4AW-3-I, RD-6AW-3-II and RD-4BW-4-I) are generally similar but the position and the distribution of the buckling ripples can be different: near the mid-height of the steel tube [see Fig. 11(a)], at a position close to one end of the steel tube [see Fig. 11(b)], or at several positions alone the height of the steel tube [see Fig. 11(c)]. In particular, for the identical specimens with wave-shaped stiffeners (i.e. RD-4BS-3-I,II), the shape and position of the buckling ripples on the two steel inner tubes are remarkably different, as shown in Figs. 11(d)-(e). The possible reasons for the difference in the buckling modes shown in Figs. 10-11 include (1) the difference of the initial geometry imperfection of the steel tubes; and (2) the slight difference of the complex interaction between the confined concrete and the steel tubes.

Fig. 12 shows the comparisons of the axial strains based on the readings of the mid-region LVDTs (i.e., 150mm mid-height shortening) and those based on the readings of the whole-length LVDTs (i.e., overall shortening) for two of the specimens of which the steel tubes buckle near the mid-height. It is shown in Fig. 12 that the axial strain based on mid-region shortening is quite close to that based on the overall shortening before the steel inner tubes buckle, while the former can be much larger than (by up to 50%) the latter in the post-buckling stage. The main reason for this observation is believed to be that for such specimens, the local buckling of the steel tubes near the mid-height led to the localization of axial deformation of the whole column therein. This indicates that the axial strains based on the readings of the mid-region LVDTs may not reasonably reflect the general behavior of the whole specimen in the post-buckling stage. As a result, for the discussions on the full-range behavior of the specimens in this paper, the axial strains based on the overall shortening are used, while for the discussions on the buckling strains of steel inner tubes and the pre-buckling behavior of specimens (i.e. the discussions in Sections 3.5 and 3.6), the axial strains based on the mid-region shortenings are used.

Typical buckling modes of the steel tubes in DSTC and R-DSTC specimens, captured by the camera (see Fig. 6) installed in the specimens at the rupture of FRP, are shown in Fig. 13. The vertical white lines in Figs. 13(b), (c) indicate the positions of the stiffeners in R-DSTC specimens, while the white lines in Fig. 13(a) represent the corresponding positions in DSTC specimens. As shown in Figs. 13(b), (c), the buckling ripples on the steel tubes in R-DSTC specimens occurred only between the stiffeners, which indicates that the stiffeners can limit the generation and propagation of the buckling ripples and thus restrain the local buckling of the steel tube to some extent.

3.2 Axial Load-Strain Behavior of Steel Tubes

The experimental axial load-strain curves of the three bare steel tubes (i.e., ST, RST-4 and RST-6) under concentric compression are compared in Fig. 14, in which the axial strains were calculated using the overall axial shortening of the steel tubes. As observed from test, the axial load peaked soon after the initiation of local buckling of the steel tube and then decreased rapidly due to the development of the local buckling. The axial strains at axial peak loads for specimens RST-4 and RST-6 (i.e., steel tubes with stiffeners) are 0.032 and 0.034, respectively, which are nearly two time of that for specimen ST (0.016 from test). This indicates that the local buckling of steel tubes can be largely delayed by the existence of stiffeners. Comparison of the descending branches shown in Fig. 14, however, reveals that the existence of stiffeners has little effect on the descending rate of the axial loads (i.e., the slope of the curves) after the local buckling of steel tubes happened. This could be mainly due to that the stiffeners bulked at the same time as the steel tubes for RST-4 and RST-6, as observed in the tests.

3.3 Axial Load-Strain Behavior of DSTCs and R-DSTCs

Comparisons of the axial load-strain curves of test specimens are shown in Figs. 15-20, in which the axial strains were based on the overall axial shortening measured by the corresponding LVDTs. As can be seen from Figs. 15-20, the axial load-strain curves of DSTC and R-DSTC specimens are generally comprised of four segments: (1) an initial ascending segment; (2) another ascending segment following the first one but with a smaller slope; (3) a descending segment following the second segment; and (4) a terminal segment which can be ascending (with a smaller slope than the second segment), descending (with a smaller descending rate than the third segment) or flat. The above four segments are all nearly linear, while the three transition regions connecting the adjacent segments are all smooth. In the initial ascending segment, the steel inner tubes is in the elastic stage, while the concrete has little lateral expansion and thus the FRP outer tubes are hardly activated yet. In the second segment, the steel inner tubes enter the inelastic stage, while the lateral expansion of concrete starts increasing rapidly and thus the FRP outer tubes are activated to provide lateral confinement to concrete. Due to the initiation of the buckling of steel tube, as recorded by the small camera installed inside the steel tube, the curves peak at the end of the second segment and then fall into the descending segment (i.e. the third segment). This descending segment is caused by the propagation of local buckling of the steel tube and the possible local crushing of concrete. The videos from the small camera showed that during the third segment, new buckling ripples occur one by one and grow rapidly; when it reaches the end of the third segment, the quantity and the size of the buckling ripples become stable and hardly change afterward. Due to the increasing FRP confinement, the dropping rate of the axial load of the third segment becomes smaller and smaller, and the axial load-strain curve gradually enter the fourth segment, which can be ascending, descending or flat, depending on the real confinement provided by the FRP outer tube to the concrete. Based on the feature of axial load-strain curves, comparisons and discussions are made with the focus on the following key data: (1) the axial load (F_p) and axial strain (ε_p) at the transition point (peak point) between the second segment and the third segment of the curves; (2) the axial load (F_n) at the transition point between the third segment and the terminal segment of the curves; (3) the axial load (F_u) and the axial strain (ε_u) at the terminal points of the curves. For each pair of identical specimens, the corresponding average results (i.e., F_p^{avg}, ε_p^{avg}, F_n^{avg}, F_u^{avg}, ε_u^{avg}) are also calculated. A parameter termed "load-decrease ratio", which is defined as $\lambda = (F_p^{avg} - F_n^{avg})/F_p^{avg}$, is used to describe the normalized magnitude of the decrease of axial load in the third segment of the curves. These key results of all the DSTC and R-DSTC specimens are summarized in Table 3. Based on the axial load-strain curves shown in Figs. 15-20 and the key results listed in Table 3, the axial load-strain behavior of DSTC and R-DSTC specimens are further discussed in the following subsections.

3.3.1 Effect of the Quantity of the Stiffeners

Fig. 15 shows the comparisons of the axial load-strain curves of D-3-I,II, RD-4AW-3-I,II and RD-6AW-3-I,II. Between these three pairs of specimens, the only difference is the quantity of stiffeners on the steel tubes. As can be seen from Fig. 15, the increase in the quantity of stiffeners leads to a higher axial loading capacity, a larger ultimate axial strains, and a smaller dropping rate of the axial load after the peak loads. This can be attributed to: (1) the increase in the amount of longitudinal steel reinforcement (i.e., more stiffeners) (2) the delayed buckling of the steel tubes (i.e., more stiffeners can restrain more effectively the inward buckling of the steel tubes) and the resulting better confinement to the concrete. The above observations and discussions are quantitatively supported by the relevant key results of D-3-I,II, RD-4AW-3-I,II and RD-6AW-3-I,II listed in Table 3. It is worth noting in Table 3 that the load-decrease ratios (λ) of D-3-I,II, RD-4AW-3-I,II and RD-6AW-3-I,II are 17.7%, 9.3% and 3.0%, respectively, which evidently indicates that R-DSTCs have much less load decrease after the peak load due to the presence of the stiffeners. Further explanations can be found in later sections where the buckling behavior of the steel tubes and the behavior of the confined concrete in DSTC and R-DSTC specimens are discussed in depth.

3.3.2 Effect of the Layout of the Stiffeners

The total cross-sectional area of the stiffeners in RD-4BW-3-I,II is 640 mm^2, which is similar to that in RD-6AW-3-I,II (i.e., 576 mm^2), but the layouts (quantities) of stiffeners in these two pairs of specimens are different. Therefore, comparisons of the axial load-strain curves of RD-4BW-3-I,II and RD-6AW-3-I,II are presented in Fig. 16 to study the effect of the layout of the stiffeners on the behavior of R-DSTCs when the total cross-sectional area of the stiffeners is similar.

As shown in Fig. 16, the first and second segments of the axial load-strain curves of RD-4BW-3-I are almost the same as those of RD-6AW-3-I, and the first and second segments of the curve of RD-4BW-3-II are almost the same as those of RD-6AW-3-II. This indicates that the layout of the stiffeners (with the same/similar total area) has little effect on behavior of R-DSTC specimens before the steel inner tube buckles. In the post-buckling stage, however, the decreasing segments of RD-6AW-3-I,II are evidently more gradual than those of RD-4BW-3-I,II and the ultimate axial strains of RD-6AW-3-I,II are also larger than those of RD-4BW-3-I,II. The above phenomenon can also be seen from the values of ε_{cu} and λ of these two pairs of specimens shown in Table 3. It should be noted that, in fact, the cross-sectional area of stiffeners in RD-6AW-3-I,II is around 10% lower than that in RD-4BW-3-I,II. Therefore, it is not unreasonable to conclude that for a given total cross-sectional area of stiffeners, a larger quantity of stiffeners can lead to a more ductile post-buckling behavior and a larger ultimate axial strain of the specimen, and thus is preferred in real applications. It should be pointed out that similar conclusion was reported by Ref. [32] in their study on square R-DSTCs.

3.3.3 Effect of the Cross-Sectional Dimensions and the Shape of the Stiffeners

Fig. 17 shows the axial load-strain curves of three pairs of specimens (i.e., D-3-I,II, RD-4AW-3-I,II and RD-4BW-3-I,II) between which the only difference is the thickness of the stiffeners, and Fig. 18 shows the axial load-strain curves of three pairs of specimens (i.e., D-3-I,II, RD-4BN-3-I,II and RD-4BW-3-I,II) between which the only difference is the width of the stiffeners. It is evidently shown in Figs. 17 and 18 that the increase in either the stiffener thickness or the stiffener width leads to an increase in the axial loading capacity as well as the axial strain at the end of the second ascending segment of the curves (ε_p) and a decrease in the load-decrease ratio (λ). As can be seen from the key results in Tables 3, the increase in stiffener thickness from 3 mm (RD-4AW-3-I,II) to 5 mm (RD-4BW-3-I,II) leads to an increase in ε_p^{avg} from 0.027 to 0.034 and a decrease in the load-decrease ratio (λ) from 9.3% to 5.4%, while the increase in stiffener width from 16 mm (RD-4BN-3-I,II) to 32 mm (RD-4BW-3-I,II) leads to an increase in ε_p^{avg} from 0.030 to 0.034 and a decrease in the load-decrease ratio (λ) from 10.4% to 5.4%.

The effect of the shape of stiffeners on the behavior of R-DSTCs is investigated through the comparison of the axial load-strain curves between RD-4BN-3-I,II and RD-4BS-3-I,II, as shown in Fig. 19. The width of the wave-shaped stiffeners of RD-4BS-3-I,II at the nadir point is 16 mm (see Fig. 2), which is equal to the width of the stiffeners of RD-4BN-3-I,II. As can be seen from Fig. 19, the axial load-strain curves of these four specimens are very close to each other except for the larger ultimate axial strain of RD-4BS3-II. Such larger ultimate axial strain may be attributed to the unique buckling mode of its steel inner tube [see Fig. 11(e)]. Therefore, it is not unreasonable to conclude that for R-DSTCs with wave-shaped stiffeners, the axial load-strain behavior is mainly dependent on the width of the stiffeners at the nadir point. It can be expected that, however, the wave-shaped stiffeners can serve as shear connectors and thus improve the bond behavior between the concrete and the steel tube in R-DSTCs.

3.3.4 Effect of the FRP Tube Thickness

The effect of FRP tube thickness on the behavior of R-DSTCs is investigated through the comparison of the axial load-strain curves between RD-4BW-3-I,II and RD-4BW-4-I,II, as shown in Fig. 20. It can be seen from Fig. 20 that the curves of RD-4BW-4-I,II are higher and longer than that of RD-4BW-3-I,II, indicating that the increase in the thickness of FRP jacket leads to an increase in both the loading capacity and axial deformation capacity of R-DSTCs. This is because for a given axial strain, a thicker FRP jacket/tube provides a higher confinement to the concrete core, and thus leads to a smaller lateral expansion of the concrete core and a higher axial stress in concrete. Although the variation of the FRP tube thickness in this study has little effect on the slopes of the first two segments of the axial load-strain curves, the slope of the terminal segment of R-DSTCs with a thicker FRP tube (i.e., RD-4BW-4-I,II) is evidently larger than that of R-DSTCs with a thinner FRP tube (i.e., RD-4BW-3-I,II), as shown in Fig. 20. This indicates that the ascending trend (if any) of the terminal segment is due to the gradual increasing FRP confinement and the slope of the terminal segment is closely related to the stiffness of the FRP outer tube. The effects of the FRP tube thickness are also quantitatively demonstrated in Table 3: an increase in the FRP tube thickness from 3 plies (RD-4BW-3-I, II) to 4 plies (RD-4BW-4-I, II), leads to an increase in the value of F_p^{avg} from 2571 kN to 2795 kN, an increase in the value of F_u^{avg} from 2477 kN to 2927 kN and an increase in the value of ε_u^{avg} from 0.078 to 0.115.

3.4 Behavior of the FRP Tubes in DSTCs and R-DSTCs

The comparisons of the axial strain-hoop strain curves of the FRP jackets in DSTCs and R-DSTCs are plotted in Fig. 21, in which the axial strains were based on the overall shortening of the specimens and the hoop strains were the average values of the readings of the three lateral strain gauges attached on the FRP jacket at mid-height (see Fig. 7).

The curves in Fig. 21 are terminated at the rupture of the FRP jackets. It can be seen from Fig. 21 that the hoop strains in the two DSTCs are similar to each other and are both larger (absolute value) than those in the R-DSTCs at the initial stage, and then the hoop strain in

D-3-II gradually becomes smaller (absolute value) than that in D-3-I and even those in the R-DSTC specimens. The smaller hoop strain of FRP in R-DSTC specimens in Fig. 21 than that of Specimens D-3-I,II at a given axial strain was due to the existence of stiffeners in the former. It is also evident from Fig. 21 that the width of the stiffeners shows a larger influence on the hoop strain of FRP than either the quantity or the thickness of the stiffeners. As can be seen from Fig. 21(d), before the buckling of steel inner tubes, the axial strain-hoop strain curves of RD-4BS-3-I,II almost coincide with those of RD-4BN-3-I,II, indicating that the "semi-circles" on the wave-shaped stiffeners have little effect on the axial strain-hoop strain behavior of the FRP outer tube before the buckling of steel tubes. Afterwards, however, the hoop strains of the former become smaller (absolute value) than the latter for a given axial strain and the gap tends to increase with the axial strain. The different axial strain-hoop strain behavior between D-3-I and D-3-II can be attributed to the different buckling locations on the steel inner tubes. As can be seen from Fig. 10, the buckling location of the steel tube in D-3-I is near the mid-height of the specimen (i.e., closer to the lateral strain gauges on FRP), while that of the steel tube in D-3-II is near the middle of the upper half part of the specimen (i.e., further to lateral strain gauges on FRP). The concentrated axial deformation caused by the buckling ripples happened near the mid-height of the steel tube of D-3-I results in a large FRP hoop strain therein and such large hoop strain was well captured by the lateral strain gauges attached nearby. The concentrated axial deformation caused by the buckling ripples on the steel tube in D-3-II, however, was located in the upper half part of the specimen, thus the corresponding large hoop strain could not be well captured by the lateral strain gauges located at the mid-height of the specimen. Therefore, after the buckling of steel tubes, the hoop strain of FRP in D-3-II was smaller than that in D-3-I for a given axial strain and the gap became larger as the axial strain increased.

3.5 Buckling Behavior of the Steel Tubes in DSTCs and R-DSTCs

The discussions in Section 3.2 have evidently indicated that the buckling strains of the stiffener-reinforced steel tubes (i.e., RST-4 and RST-6) are much larger (by around 100%) than that of the corresponding steel tube without stiffener (i.e., ST). It is thus not unreasonable to expect that the buckling strains of the steel tubes in R-DSTCs are also larger than those of the steel tubes in the corresponding DSTC specimens. In the present study, the buckling of the steel inner tubes in DSTC and R-DSTC specimens during the test was monitored by the camera (see Fig. 6) inside the steel inner tubes, and the corresponding axial load (buckling load F_b) and axial strain (buckling strain ε_b) can be easily found as the recorded videos were well synchronized with other test results (e.g. axial load and strain) obtained from the data loggers of the compression test machine. It should be noted that the buckling strains in Table 4 were all based on the 150 mm mid-region shortening of the specimens as mentioned earlier. The key results are listed in Table 4, with F_b^{avg} and ε_b^{avg} being respectively the average buckling load and average buckling strain for each pair of identical specimens. It should be noted that the results of D-3-II are not available, as the camera in D-3-II unexpectedly stopped working soon after the start of test. Therefore only the results of D-3-I are used in the following comparisons and discussions. Based on the results listed in Table 4, the following observations and conclusions can be obtained: (1) the buckling strain of steel tubes in all the R-DSTCs are larger than that in the D-3-I by 33.3% to 66.7%; (2) either a wider or a thicker stiffener results in a larger buckling strain, as can be seen from the comparison between RD-4AW-3-I,II and RD-4BW-3-I,II and the comparison between RD-4BN-3-I,II and RD-4BW-3-I,II; (3) an increase in the quantity of stiffeners leads to an increase in buckling strains, as can be seen from the comparison between RD-4AW-3-I,II and RD-6AW-3-I,II; (4) the variation of the quantity of stiffeners has marginal effect on the buckling strain of the steel tubes in R-DSTCs if the total cross-sectional area of the stiffeners is similar, as can be seen from the comparison between RD-4BW-3-I,II and RD-6AW-3-I,II; (5) the existence of additional “semi-circles” (i.e., the part that forms the waves) on the wave-shaped stiffeners have nearly no effect on the buckling load and buckling strain of R-DSTCs, as indicated by the comparison between RD-4BN-3-I,II and RD-4BS-3-I,II; and (6) an increase in the FRP jacket thickness leads to an increase in both the buckling load and buckling strain, as can be seen from the comparison between RD-4BW-3-I,II and RD-4BW-4-I,II.

3.6 Compression Behavior of the Confined Concrete in R-DSTCs

Since it is difficult to directly measure the axial load-strain behavior of the confined concrete in the test, the axial load-strain behavior of the confined concrete is studied by properly decomposing the axial load on the R-DSTCs into several parts for comparison and analysis in this study. The axial load of R-DSTCs at a given axial strain can be approximately divided into three parts: (1) Part-1: the axial load carried by the corresponding DSTC specimen (ideally, the area taken up by the stiffeners of the R-DSTC specimen should be excluded from the concrete area); (2) Part-2: the axial load carried by the stiffeners; (3) Part-3: the additional axial load carried by the confined concrete, if any, due to the composite action (i.e., interaction between FRP, steel and concrete) in R-DSTCs. For a given R-DSTC specimen, once the Part-1 and Part-2 of the axial load are obtained, Part-3 can then be investigated by the comparison between the total axial load on the given R-DSTC specimen and the sum of Part-1 and Part-2. It should be noted that the axial load carried by the welding lines between the stiffeners and the steel tube is negligible as the welding lines are not completely continuous (with several tiny gaps) along the specimens. In the present study, for a given axial strain, Part-1 of the axial load was obtained by using the test axial load-strain curve of the DSTC specimen D-3-I, and Part-2 was calculated using the stress-strain relationships of the stiffeners obtained from the coupon tensile.

The sum of Part-1 and Part-2 versus axial strain curves are plotted in Fig. 22, where the axial load-strain curves of Specimen D-3-I and four pairs of R-DSTC specimens (i.e., RD-4AW-3-I,II, RD-6AW-3-I,II, RD-4BW-3-I,II, RD-4-BN-3-I,II) are also plotted for comparison. It should be noted that the axial strains in Fig. 22 are also all based on the 150 mm mid-region shortening of the specimens. In Fig. 22, the calculated sum curves have the same ultimate axial strain as Specimen D-3-I, while the curves obtained from test were terminated at the bucking strain of the steel inner tubes. As can be seen from Fig. 22, all curves have two linear ascending segments with a smooth transition region, and the second segments of the test curves of all the R-DSTC specimens are higher than the corresponding calculated sum curves. A further inspection of the curves shown in Fig. 22 indicates that at the terminal axial strains of the sum curve (i.e., the ultimate axial strain of D-3-I from test), the average gap of axial load between each pair of R-DSTCs and the corresponding calculated sum curve is 80-140 kN. Such gap of axial load corresponds to an axial stress of 3.5-6.1 MPa on the confined concrete, which is approximately 9.1%-15.9% of the cylinder strength of unconfined concrete in the present study. The above phenomenon indicates that the composite action between the three components in the column (i.e., FRP, steel tube and concrete) can be enhanced by the existence of stiffeners and thus additional axial load can be gained (i.e., the above-mentioned Part-3 of the axial load exists) before the buckling of the steel inner tubes. It is not unreasonable to believe that such additional axial load is mainly due to the additional confinement onto the concrete caused by the enhanced composite action. Furthermore, it should be noted that in the calculation of Part-1 in the present study, the cross-sectional area taken up by the stiffeners was not deduced from the total concrete area of Specimen D-3-I, as such deduction was very difficult to carry out accurately. This implies that the above-mentioned gap of axial load between the two nominally identical R-DSTC specimens and the corresponding calculated sum curve was underestimated to some extent. A rough calculation shows that the axial load carried by the concrete in the area taken up by the stiffeners is less than 2% of the axial load of Specimen D-3-I (i.e., less than 40 kN), because the total cross-sectional area of the stiffeners (for all the R-DSTC specimens in this study) is less than 4% of the total concrete area of D-3-I and the axial load on the annular concrete core of D-3-I is around 50% of the total axial load on D-3-I.

The above discussions indicate that compared to the corresponding DSTC specimen, the concrete in an R-DSTC specimen is better confined due to the presence of the steel stiffeners. One of the possible reasons for this phenomenon is that the stiffness of steel inner tube is enhanced by the vertical stiffeners, and thus the steel tube can provide a higher confinement to the concrete. To explore the complex composite actions in R-DSTCs, advanced approaches such as sophisticated finite element modelling are needed in future studies.

4 CONCLUSIONS

This paper presents an experimental study on the compressive behaviour FRP-concrete-steel double-skin tubular columns (DSTCs) of which the steel inner tubes are reinforced with longitudinal stiffeners. The studied parameters included the quantity of the stiffeners, the dimensions of the stiffeners (i.e. width and thickness), the shape of the stiffeners (i.e. rectangular and wave-shaped) and the thickness of the FRP jacket. Bare steel tubes (both with and without stiffeners) and normal DSTCs (without stiffeners) were also tested for comparison. Based on the test results and the discussions, the following conclusions can be drawn:

1. The buckling strain of the bare steel tubes reinforced with stiffeners is much larger (by around 100% in the present study) compared to that of the corresponding bare steel tube without stiffeners, and the buckling strain of steel tubes in R-DSTCs is also much larger (by 33.3%-66.7% in the present study) than that in the corresponding DSTCs due to the presence of stiffeners. Such effects are found to increase with the quantity, width or thickness of the stiffeners. Furthermore, it is not unreasonable to expect that the effect of stiffeners is more appreciable in R-DSTCs with a relatively thin steel tube. The effect of diameter to thickness ratio of the steel tube on the behaviour of R-DSTCs can be an interesting issue to be addressed in future studies.

2. Compared with the corresponding DSTCs, R-DSTCs have a higher axial loading capacity, a larger ultimate axial strain and a more ductile axial load-strain behavior. The increase in the quantity, width or thickness of the stiffeners can enhance the superior behavior of R-DSTCs. When the total cross-sectional area of the stiffeners on an R-DSTC is kept constant, the increase in the quantity of stiffeners (which will result in decrease in the width or thickness of the stiffeners) can lead to a more ductile post-peak behavior of the R-DSTC.

3. Although the “semi-circles” on the wave-shaped stiffeners can be expected to improve the bond behavior between the concrete and the steel tube, the existence of such additional “semi-circles” shows marginal effect on the behavior of R-DSTCs subjected to concentric compression in the present study, compared with R-DSTCs in which the flat

stiffeners with the same width as that of the wave-shaped stiffeners at the nadir point are used.

4. For a given axial strain, the hoop strain of the FRP outer tube in an R-DSTC is smaller than that in the corresponding DSTC. The increase in the width of stiffeners is found to be more effective in reducing the hoop strain of the FRP outer tube in an R-DSTC than the increase in either the quantity or the thickness of stiffeners for a given axial strain of the specimen.

5. The presence of stiffeners in an R-DSTC can enhance the composite action between the three components of the specimen (i.e., FRP, steel tube and concrete) compared with the corresponding DSTC, and such enhanced composite action introduces additional/better confinement onto the concrete and thus leads to a higher axial load of the specimen.

ACKNOWLEDGEMENT

The authors gratefully acknowledge the financial support provided by the Australian Research Council through its Discovery Projects funding scheme (project ID: DP170102992).

5 REFERENCES

[1] Mirmiran, A. and Shahawy, M. Behavior of concrete columns confined by fiber composites. Journal of Structural Engineering 1997; 123(5):583-590.

[2] Fam, A. and Rizkalla, S.H. Behavior of axially loaded concrete-filled circular FRP tubes. ACI Structural Journal 2001; 98(3):280-289.

[3] Teng, J.G., Chen, J.F., Smith, S.T. and Lam, L. FRP-strengthened RC structures. John Wiley; 2002.

[4] Hollaway, L.C. and Teng, J.G. Strengthening and rehabilitation of civil infrastructures using fibre-reinforced polymer (FRP) composites. Woodhead Publishing; 2008.

[5] Teng, J.G., Yu, T. and Fernando, D. Strengthening of steel structures with fiber-reinforced

polymer composites", Journal of Constructional Steel Research 2012; 78:131-143.

[6] Yu, T., Zhang, S.S., Huang, L. and Chan, C. Compressive behavior of hybrid double-skin tubular columns with a large rupture strain FRP tube. Composite Structures 2017; 171:10-18.

[7] Yu, T., Zhao, H.C., Ren, T. and Remennikov, A. Novel hybrid FRP tubular columns with large deformation capacity: Concept and behaviour. Composite Structures 2019; 212:500-512.

[8] Zhao, J.L., Xu, C., Sun, L. and Wu, D. Behaviour of FRP-confined compound concrete–filled circular thin steel tubes under axial compression. Advances in Structural Engineering 2020; 1369433219900941.

[9] Zeng, J.J., Duan, Z.J., Guo, Y.C., Xie, Z.H. and Li, L.J. Novel fiber-reinforced polymer cross wrapping strengthening technique: A comparative study. Advances in Structural Engineering 2020; 23(5):979-996.

[10] Teng, J.G., Yu, T., Wong, Y.L. and Dong, S.L. Hybrid FRP–concrete–steel tubular columns: concept and behavior. Construction and Building Materials 2007; 21(4):846-854.

[11] Karimi, K., Tait, M.J. and El-Dakhakhni, W.W. Testing and modeling of a novel FRP-encased steel–concrete composite column. Composite Structures 2011; 93(5):1463-1473.

[12] Ozbakkaloglu, T. and Lim, J.C. "Axial compressive behavior of FRP-confined concrete: Experimental test database and a new design-oriented model", Composites Part B: Engineering 2013; 55:607-634.

[13] Yu, T., Lin, G. and Zhang, S.S. Compressive behavior of FRP-confined concrete-encased steel columns. Composite Structures 2016; 154:493-506.

[14] Yu, T., Chan, C., Teh, L. and Teng, J.G. Hybrid FRP-concrete-steel multitube concrete columns: concept and behavior. Journal of Composites for Construction 2017; 21(6):04017044.

[15] Huang, L., Zhang, S.S., Yu, T. and Wang, Z.Y. Concrete-encased steel columns confined with large rupture strain FRP composites: axial compression tests. Proceedings of the 24th Australian Conference on the Mechanics of Structures and Materials (ACMSM24),

Perth, 6–9 December, 2016.

[16] Huang, L., Yu, T., Zhang, S.S. and Wang, Z.Y. FRP-confined concrete-encased cross-shaped steel columns: Concept and behavior. Engineering Structures 2017; 152:348-358.

[17] Huang, L., Zhang, S.S., Yu, T. and Wang, Z.Y. Compressive behaviour of large rupture strain FRP-confined concrete-encased steel columns. Construction and Building Materials 2018; 183:513-522.

[18] Teng, J.G., Wang, Z., Yu, T., Zhao, Y. and Li, L.J. Double-tube concrete columns with a high-strength internal steel tube: concept and behaviour under axial compression. Advances in Structural Engineering 2018; 21(10):1585-1594.

[19] Chan, C.W., Yu, T., Zhang, S.S. and Xu, Q.F. Compressive behaviour of FRP-confined rubber concrete. Construction and Building Materials 2019; 211:416-426.

[20] Wong, Y.L., Yu, T., Teng, J.G. and Dong, S.L. Behavior of FRP-confined concrete in annular section columns. Composites Part B: Engineering 2008; 39(3):451-466.

[21] Yu, T., Teng, J.G. and Wong, Y.L. Stress-strain behavior of concrete in hybrid FRP-concrete-steel double-skin tubular columns. Journal of structural engineering 2009; 136(4):379-389.

[22] Yu, T., Wong, Y.L. and Teng, J.G. Behavior of hybrid FRP-concrete-steel double-skin tubular columns subjected to eccentric compression. Advances in Structural Engineering 2010; 13(5):961-974.

[23] Yu, T., Teng, J.G., Wong, Y.L. and Dong, S.L. Finite element modeling of confined concrete-II: Plastic-damage model. Engineering structures 2010; 32(3):680-691.

[24] Ozbakkaloglu, T. and Fanggi, B.L. Axial compressive behavior of FRP-concrete-steel double-skin tubular columns made of normal-and high-strength concrete. Journal of Composites for Construction 2013; 18(1):04013027.

[25] Ozbakkaloglu, T. and Idris, Y. Seismic behavior of FRP-high-strength concrete–steel double-skin tubular columns. Journal of Structural Engineering 2014; 140(6): 04014019.

[26] Zhang, B., Teng, J.G. and Yu, T. Experimental behavior of hybrid FRP–concrete–steel double-skin tubular columns under combined axial compression and cyclic lateral

loading. Engineering Structures 2015; 99:214-231.

[27] GB 50608-2010. Technical code for infrastructure application of FRP composites. China Metallurgical Construction Association; 2010.

[28] Shams, M. and Saadeghvaziri, M.A. State of the art of concrete-filled steel tubular columns. Structural Journal 1997; 94(5):558-571.

[29] Tao, Z., Han, L.H. and Wang, Z.B. Experimental behaviour of stiffened concrete-filled thin-walled hollow steel structural (HSS) stub columns. Journal of Constructional Steel Research 2005; 61(7):962-983.

[30] Tao, Z., Han, L.H. and Wang, D.Y. Experimental behaviour of concrete-filled stiffened thin-walled steel tubular columns. Thin-Walled Structures 2007; 45(5):517-527.

[31] Zhu, A., Zhang, X., Zhu, H., Zhu, J. and Lu, Y. Experimental study of concrete filled cold-formed steel tubular stub columns. Journal of Constructional Steel Research 2017; 134:17-27.

[32] Peng, K.D., Yu, T., Hadi, M.N. and Huang, L. Compressive behavior of hybrid double-skin tubular columns with a rib-stiffened steel inner tube. Composite Structures 2018; 204:634-644.

[33] Anggawidjaja, D., Ueda, T., Dai, J.G. and Nakai, H. Deformation capacity of RC piers wrapped by new fiber-reinforced polymer with large fracture strain. Cement and Concrete Composites 2006; 28(10):914-927.

[34] Dai, J.G., Bai, Y.L. and Teng, J.G. Behavior and modeling of concrete confined with FRP composites of large deformability. Journal of Composites for Construction 2011; 15(6):963-973.

[35] Abdelkarim, O.I. and ElGawady, M.A. Concrete-Filled-Large Deformable FRP Tubular Columns under Axial Compressive Loading. Fibers 2015; 3(4):432-449.

[36] Bai, Y.L., Dai, J.G. and Teng, J.G. Cyclic compressive behavior of concrete confined with large rupture strain FRP composites. Journal of Composites for Construction 2013; 18(1):04013025.

[37] Bai, Y.L., Dai, J.G., Mohammadi, M., Lin, G. and Mei, S.J. Stiffness-based design-oriented compressive stress-strain model for large-rupture-strain (LRS) FRP-confined concrete. Composite Structures 2019; 223:110953.

[38] AS 1012.9. Methods of testing concrete-Determination of the compressive strength of concrete specimens, Standards Australia; 2014.

[39] BS18. Method for tensile testing of metals (including aerospace materials). British Standards Institution; 1987.

[40] ASTM, D3039/D3039M. Standard test method for tensile properties of polymer matrix composite materials, ASTM Committee D30; 2014.

[41] Shahawy, M., Mirmiran, A. and Beitelman, T. Tests and modeling of carbon-wrapped concrete columns. Composites Part B: Engineering 2000; 31(6):471-480.

Table 1. Test matrix

Specimen	Diameter (mm)	Steel tube outer diameter/thickness (mm)	Height (mm)	FRP plies	Dimensions of stiffeners (mm)		Quantity of stiffeners
					Thickness	Width	
D-3-I, II	240	168.4/4.8	600	3	N/A	N/A	N/A
RD-4AW-3-I,II				3	3	32	4
RD-6AW-3-I,II				3	3	32	6
RD-4BW-3-I,II				3	5	32	4
RD-4BW-4-I,II				4	5	32	4
RD-4BN-3-I, II				3	5	16	4
RD-4BS-3-I, II				3	5	peak 32, nadir 16	4
ST	N/A	168.4/4.8	600	N/A	N/A	N/A	N/A
RST-4					5	32	4
RST-6					5	32	6

Table 2. Material properties

Concrete	Elastic modulus	Compressive strength (MPa)	Strain at peak stress	
	N/A	36.9	0.0025	
Steel	Type/thickness (mm)	Elastic modulus (GPa)	Yield strength (MPa)	Ultimate strength (MPa)
	flat bar/3.0	203.8	342.5	438.3
	flat bar/5.0	216.4	347.4	510.3
	Steel tube/4.8	201.6	406.5	462.8
PET-FRP	N/A	Tensile strength (MPa)	Rupture strain	
		928.1	0.0981	

Table 3. Key test results

Specimen	F_p (kN)	F_p^{avg}	ε_p	ε_p^{avg}	F_n (kN)	F_n^{avg}	F_u (kN)	F_u^{avg}	ε_u	ε_u^{avg}	$\lambda = (F_p^{avg} - F_n^{avg})/F_p^{avg}$ (%)
D-3-I	2061	2079	0.023	0.026	1703	1710	1715	1772	0.062	0.073	17.7
D-3-II	2096		0.028		1716		1828		0.083		
RD-4AW-3-I	2418	2410	0.029	0.027	2172	2186	2200	2242	0.087	0.089	9.3
RD-4AW-3-II	2401		0.025		2200		2283		0.091		
RD-4BW-3-I	2504	2571	0.030	0.034	2382	2433	2466	2477	0.084	0.078	5.4
RD-4BW-3-II	2637		0.037		2483		2487		0.072		
RD-4BW-4-I	2843	2795	0.041	0.037	2678	2613	2981	2927	0.129	0.115	6.5
RD-4BW-4-II	2747		0.032		2547		2873		0.101		
RD-4BN-3-I	2419	2442	0.028	0.030	2170	2189	2105	2172	0.072	0.074	10.4
RD-4BN-3-II	2465		0.031		2208		2239		0.076		
RD-4BS-3-I	2414	2410	0.027	0.027	2215	2186	2252	2132	0.071	0.088	9.3
RD-4BS-3-II	2406		0.027		2156		2012		0.105		
RD-6AW-3-I	2505	2593	0.039	0.038	2437	2514	2534	2566	0.088	0.103	3.0
RD-6AW-3-II	2681		0.037		2590		2598		0.118		

Note: F_p and ε_p are the axial load and axial strain at the transition point (peak point) between the second segment and the third segment of the curves, respectively; F_n is the axial load at the transition point between the third segment and the terminal segment of the curves; F_u and ε_u are the axial load and the axial strain at the terminal points of the curves, respectively; λ is the so-called 'load-decrease ratio' as defined in the table; F_p^{avg}, ε_p^{avg}, F_n^{avg}, F_u^{avg}, ε_u^{avg} are the average values of F_p, ε_p, F_n, F_u, ε_u of the each pair of nominally identical specimens, respectively.

Table 4. Buckling load and buckling strain of the specimens.

Specimen	Buckling load F_b (kN)	F_b^{avg}	Buckling strain ε_b	ε_b^{avg}
D-3-I	2034	2043	0.018	0.018
D-3-II	--		--	
RD-4AW-3-I	2401	2391	0.026	0.024
RD-4AW-3-II	2381		0.022	
RD-4BW-3-I	2488	2523	0.027	0.028
RD-4BW-3-II	2557		0.028	
RD-4BW-4-I	2794	2756	0.033	0.030
RD-4BW-4-II	2717		0.027	
RD-4BN-3-I	2393	2407	0.024	0.025
RD-4BN-3-II	2421		0.025	
RD-4BS-3-I	2405	2403	0.025	0.025
RD-4BS-3-II	2400		0.025	
RD-6AW-3-I	2409	2533	0.023	0.028
RD-6AW-3-II	2657		0.033	

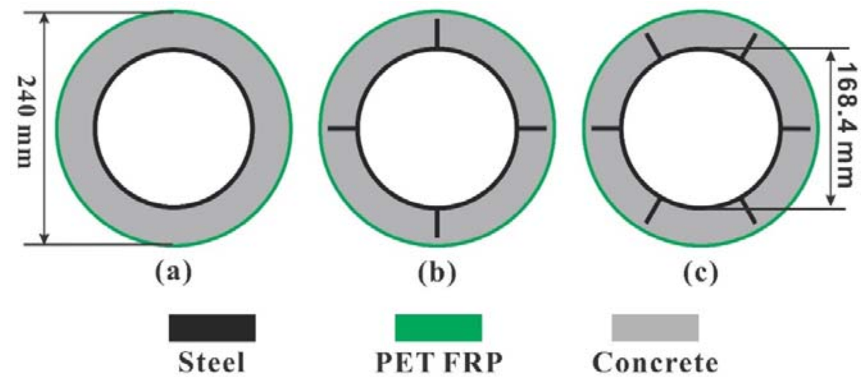

Figure 1. Schematic diagrams of cross-sectional configurations for: (a) DSTC specimens, (b) R-DSTC specimens with four stiffeners and (c) R-DSTC specimens with six stiffeners

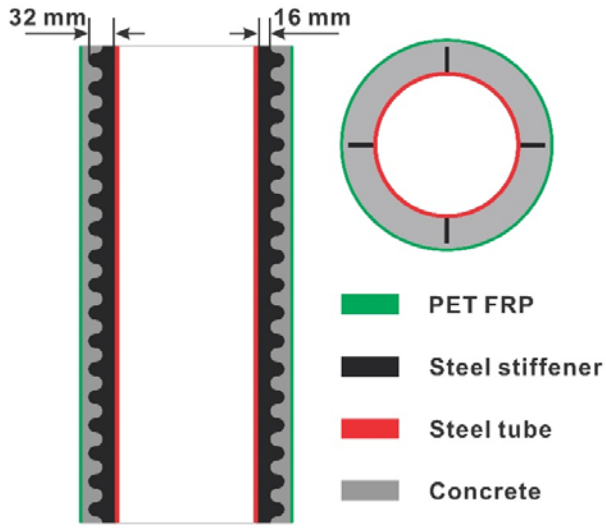

Figure 2. The configuration and dimensions of the “wave-shaped” stiffeners in Specimens RD-4BS-3-I, II

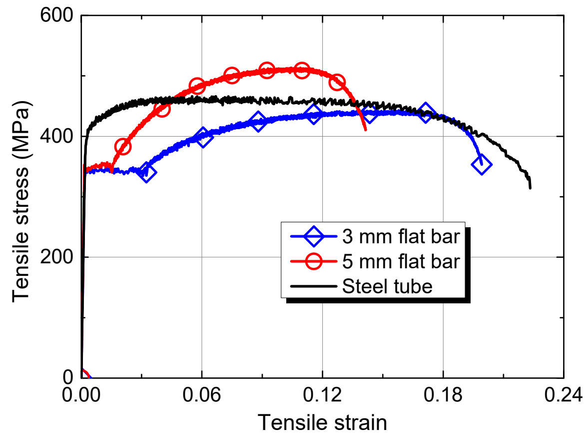

Figure 3. Tensile stress-strain curves of steel

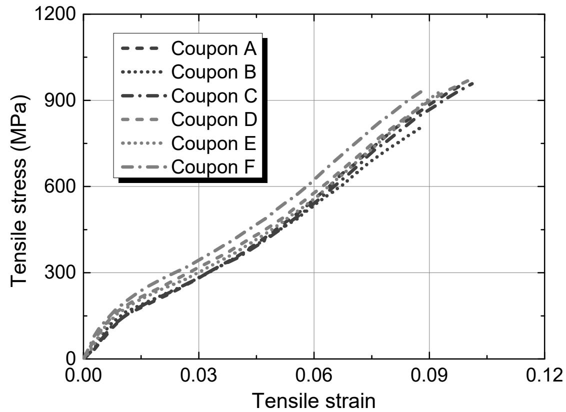

Figure 4. Tensile stress-strain curves of PET FRP

Figure 5. DSTC and R-DSTC specimens in preparation

.

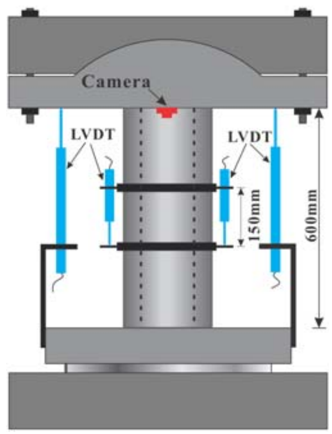

Figure 6. Schematic diagram of the test set-up

.

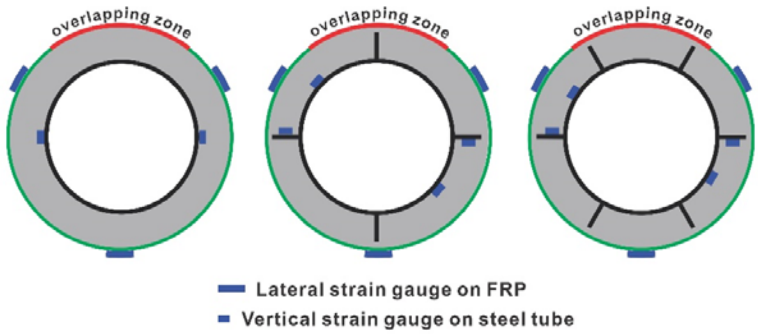

Figure 7. Layout of strain gauges on DSTC and R-DSTC specimens

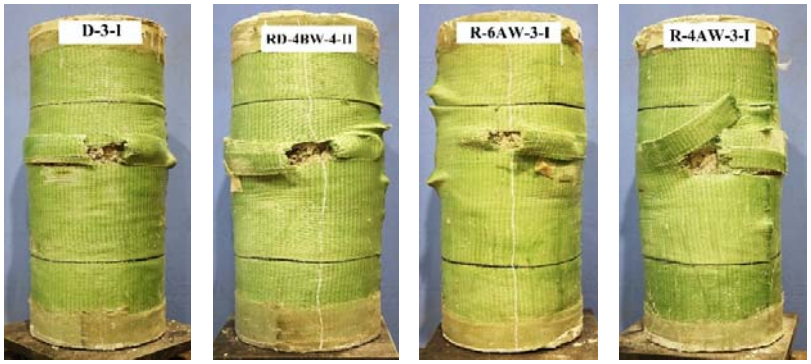

(a) (b) (c) (d)

Figure 8. Typical failure modes of DSTC and R-DSTC specimens

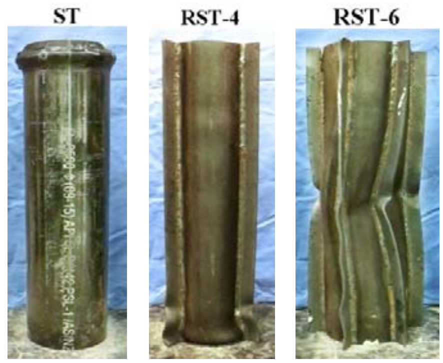

(a) (b) (c)

Figure 9. Failure modes of bare steel tubes under axial compression

(a) (b)

Figure 10. Failure modes of steel tubes in DSTC specimens

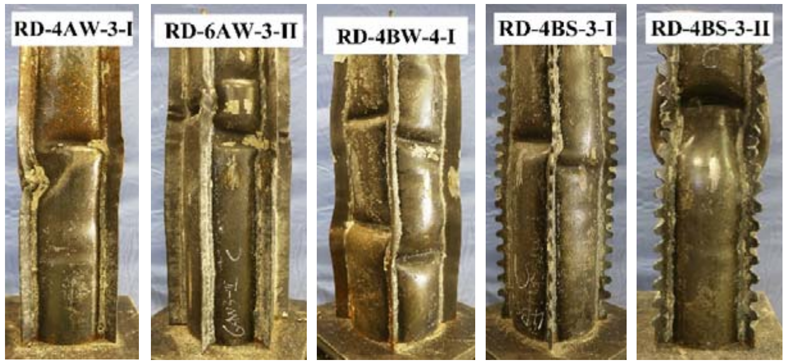

(a) (b) (c) (d) (e)

Figure 11. Typical failure modes of steel inner tubes in R-DSTC specimens

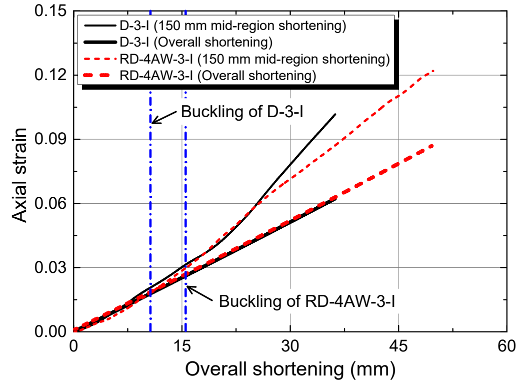

Figure 12. Comparison of axial strains calculated from the overall shortening and the 150 mm mid-region shortening

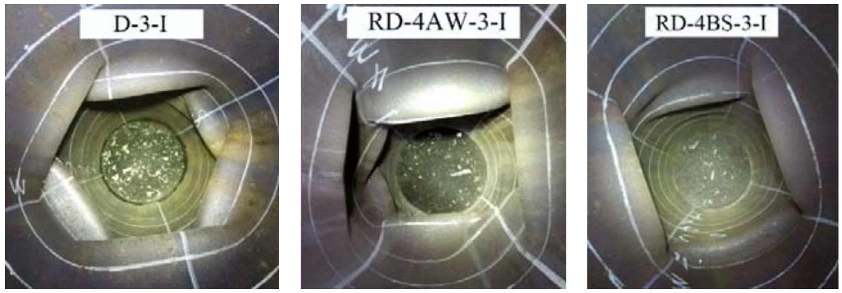

(a) (b) (c)

Figure 13. Inside view of steel inner tubes at the failure of specimen

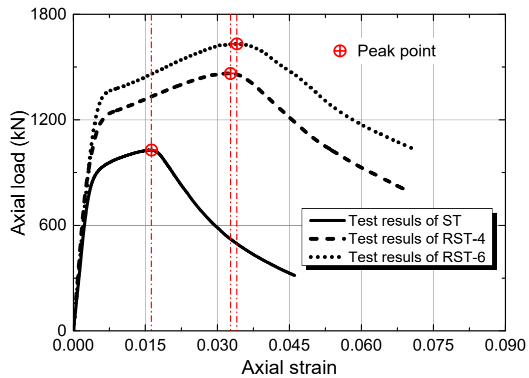

Figure 14. Axial load-strain curves of bare steel tubes under compression

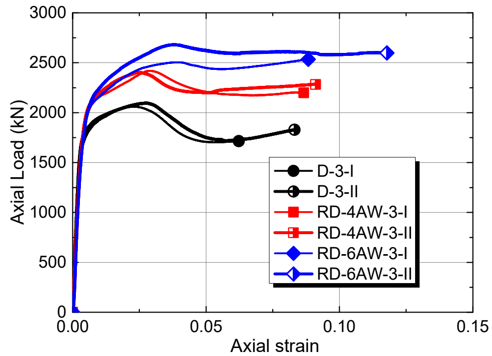

Figure 15. Effect of the quantity of stiffeners on the axial load-strain behavior of R-DSTCs

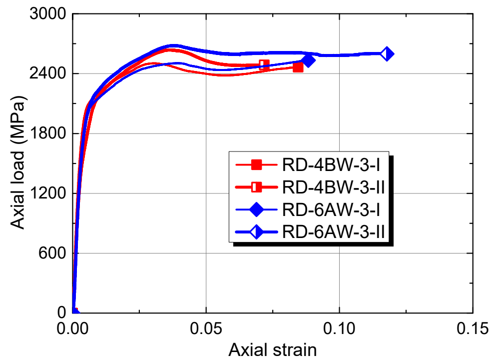

Figure 16. Effect of the layout of stiffeners (with a similar total cross-sectional area) on the axial load-strain behavior of R-DSTCs

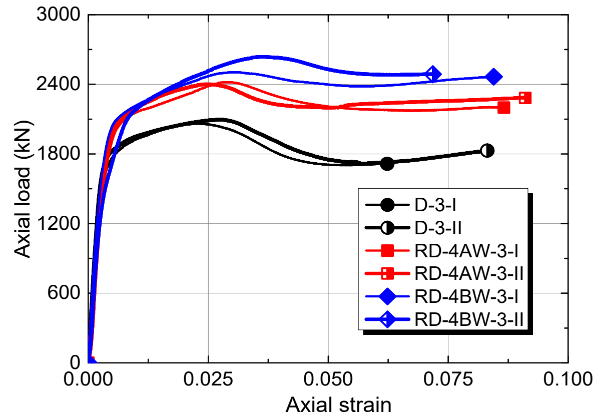

Figure 17. Effect of the thickness of stiffeners on the axial load-strain behavior of R-DSTCs

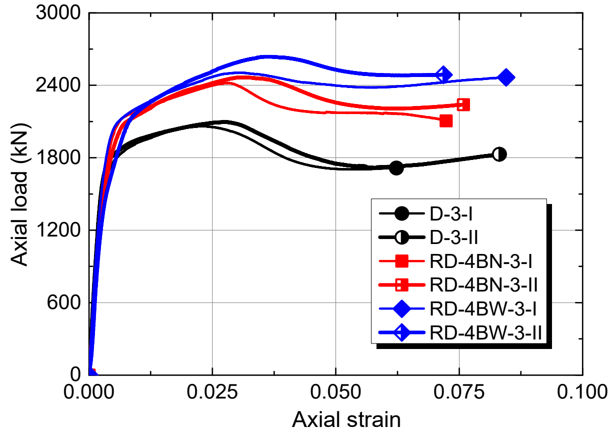

Figure 18. Effect of the width of stiffeners on the axial load-strain behavior of R-DSTCs

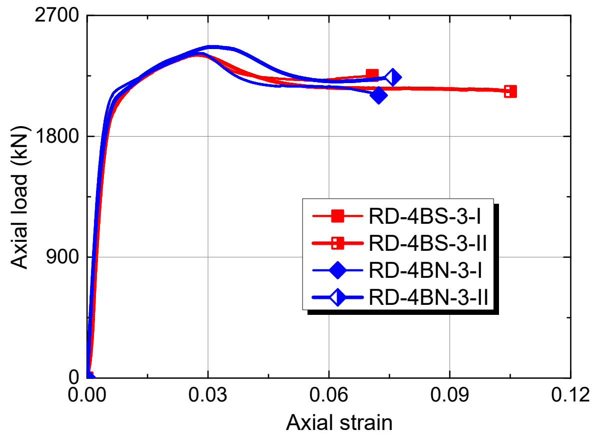

Figure 19. Effect of the shape of stiffeners on the axial load-strain behavior of R-DSTCs

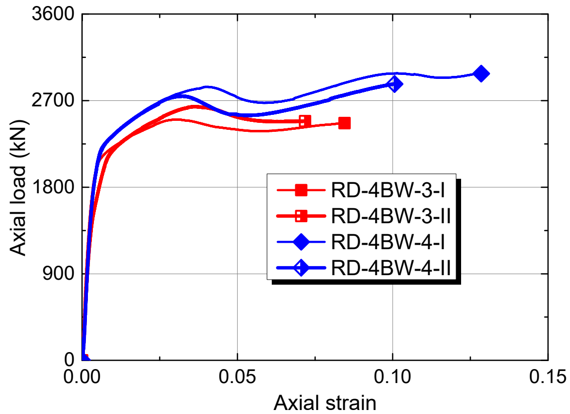

Figure 20. Effect of FRP tube thickness on the axial load-strain behavior of R-DSTCs

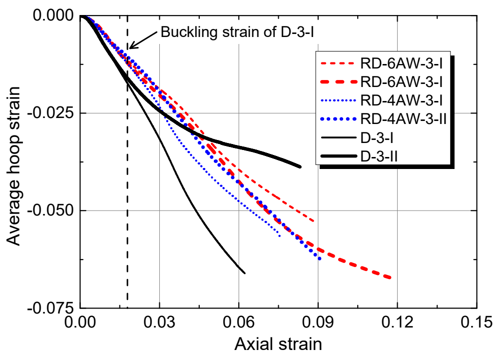

(a) Effect of the quantity of stiffeners

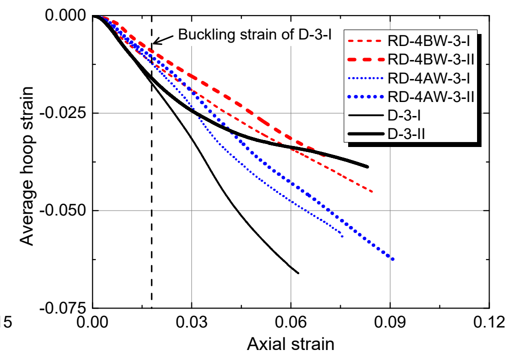

(b) Effect of the thickness of stiffeners

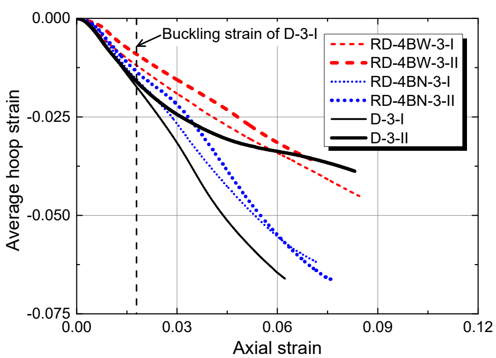

(c) Effect of the width of stiffeners

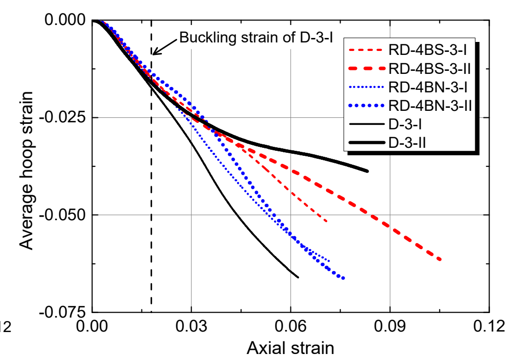

(d) effect of the shape of stiffeners

Figure 21. Axial strain-hoop strain curves of the FRP tubes in DSTCs and R-DSTCs

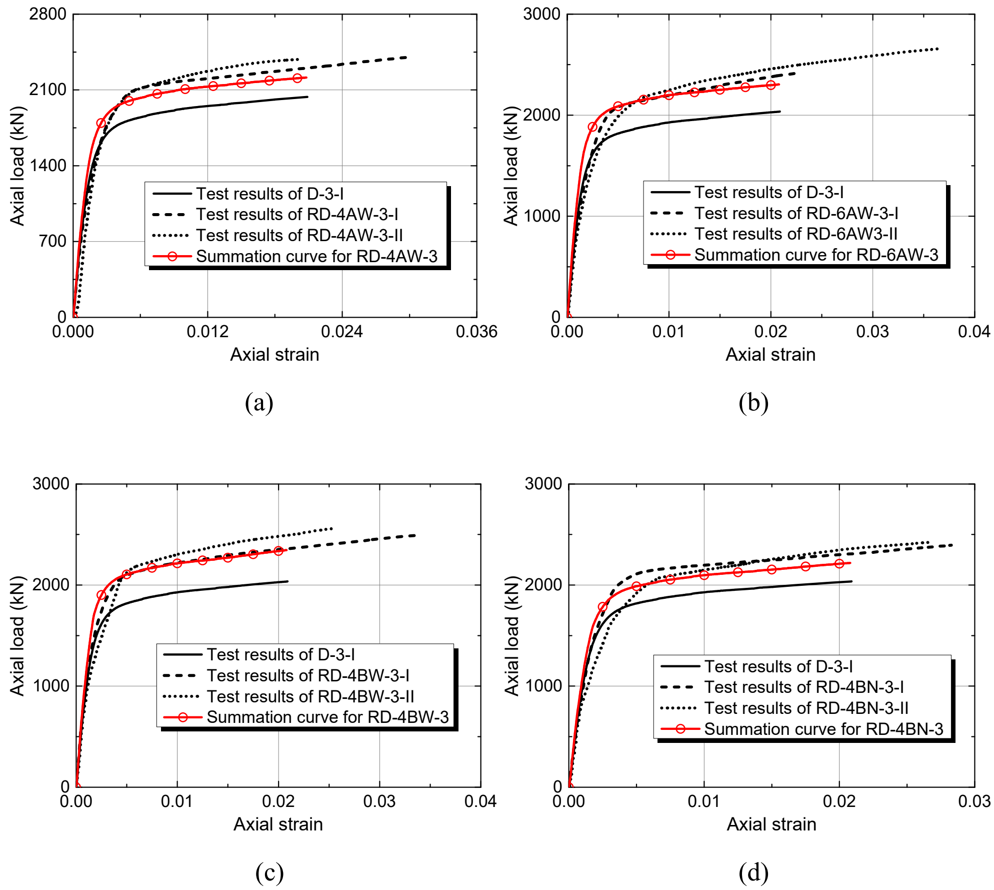

Figure 22. Axial load-strain curves: test result versus simple summation